Optimizing oxygen transport through $La_{0.6}Sr_{0.4}Co_{0.2}Fe_{0.8}O_{3-\delta}$ hollow fiber by microstructure modification and Ag/Pt catalyst deposition

ARTICLE *in* ENERGY & FUELS · AUGUST 2012

Impact Factor: 2.79 · DOI: 10.1021/ef300542e

energy&fuels

Article

pubs.acs.org/EF

Optimizing Oxygen Transport Through $La_{0.6}Sr_{0.4}Co_{0.2}Fe_{0.8}O_{3-\delta}$ Hollow Fiber by Microstructure Modification and Ag/Pt Catalyst Deposition

Dezhi Han,[†,‡] Jaka Sunarso,[§] Xiaoyao Tan,[∥] Zifeng Yan,*[,†] Lihong Liu,[‡] and Shaomin Liu*[,‡]

[†]State Key Laboratory of Heavy Oil Processing, CNPC Key Laboratory of Catalysis, China University of Petroleum, Qingdao 266555, China

[‡]Department of Chemical Engineering, Curtin University, Perth, Western Australia 8645, Australia

[§]Australian Research Council (ARC) Centre of Excellence for Electromaterials Science, Institute for Frontier Materials, Deakin University, Burwood, Victoria 3125, Australia

[∥]School of Chemical Engineering, Shandong University of Technology, Zibo 255049, China

ABSTRACT: This work compares the oxygen permeation fluxes of five different $La_{0.6}Sr_{0.4}Co_{0.2}Fe_{0.8}O_{3-\delta}$ membranes (e.g. disk, conventional hollow fiber, modified hollow fiber, Ag- or Pt-deposited hollow fiber membranes) to elucidate the dominance of a particular oxygen transport limiting step (e.g., bulk-diffusion or surface reaction) within each of these membranes. At 900 °C and 100 mL min^{-1} helium gas sweep rate, the oxygen fluxes for disk, conventional hollow fiber, modified hollow fiber, Ag-deposited modified hollow fiber, and Pt-deposited modified hollow fiber membranes are 0.10, 0.33, 0.84, 1.42, and 2.62 mL min^{-1} cm^{-2}, respectively, denoting enhanced performance in this sequential order. More than 300% enhancement of fluxes is evidenced by modifying the geometry from disk to conventional hollow fiber. This is attributed to the thickness reduction from ∼1 mm to ∼0.3 mm, thus implying bulk-diffusion and surface reaction as the jointly limiting transport step for this disk membrane. In contrast to a conventional hollow fiber that has a sandwich cross-sectional structure (e.g. dense center layer sandwiched by two finger-like layers) as well as dense outer and inner circumference surfaces, the modified hollow fiber has only one dense layer in its outer circumference surface with finger-like porous layer extending all the way from outer cross-sectional part to the inner cross-sectional part. This microstructural difference, in turn, provides substantial reduction of membrane thickness and enlarges surface reaction area for modified hollow fiber (relative to conventional hollow fiber), both of which contributes to the reduced bulk-diffusion and surface reaction resistance; evidenced by almost 250% oxygen flux enhancement. To enhance the performance even further, catalyst (e.g., Ag or Pt) deposition on the outer circumference surface of modified hollow fiber can be utilized to reduce its dominating surface reaction resistance. While both catalysts increase the oxygen fluxes, Pt reveals itself as the better candidate relative to Ag due to melting-induced aggregation and growth of Ag at ∼950 °C.

1. INTRODUCTION

Oxygen production by air separation is of vital importance for many environmental and industrial processes, as most large scale clean energy technologies require oxygen as the oxidant. For example, when pure oxygen instead of air is used in power plants, the major constituent of the waste gas produced during the combustion process would be CO_2, which can be readily and economically captured. This is reflected by several big projects on oxyfuel combustion such as CS Callide (Australia), Vattenfal (German), OXY-CFB-300 (Spain) and Future Gen2 (U.S.A.) with each of them attracting billion dollar investments. However, all these oxyfuel combustion projects are still in the demonstration stage and cannot compete commercially with the conventional air-fired power plants because of the significantly high investment and operation costs related to the pure oxygen production cost via the expensive cryogenic process. Oxygen ionic transport membrane has rapidly become an attractive technology to produce oxygen from air as indicated by multimillion dollar worth research alliances in leading countries.[1] Unlike the default cryogenic process, which involves cooling air to below nitrogen's boiling point, the oxygen ionic transport membrane relies on the presence of oxygen anion vacancies at high temperature (e.g., in excess of 500 °C) and the oxygen ions hopping between these vacancies to facilitate electrochemical transport of oxygen through the membrane.[2,3] This, in turn, endows the latter technology its advantages such as lower energy consumption (relative to the cryogenic process), absolute selectivity (only oxygen passes through the membranes), and heat integration opportunities, widely available in power plants. Ionic transport membrane technology is therefore envisaged to replace the cryogenics and reduce O_2 production cost by 35% or more, offering the potential to tackle these energy penalties and improve the viability of zero emission technology.[4] Nonetheless, wide application of this technology is being hindered by high temperature sealing problem and inadequate oxygen fluxes of thick-tubular and disk membranes. To this end, hollow fiber membranes with thin wall layer have been devised as a way to address these limitations since these membranes provide a high surface area to volume ratio and require only small sealing areas on the fiber ends.

The emerging interest on hollow fiber configurations can perhaps be best evidenced by the production of hollow fibres utilizing numerous oxygen selective perovskite family compo-

Received: March 30, 2012
Revised: July 6, 2012
Published: July 9, 2012

dx.doi.org/10.1021/ef300542e | *Energy Fuels* 2012, 26, 4728−4734

sitions, for example, $BaBi_{0.05}Sc_{0.1}Co_{0.85}O_{3-\delta}$ (BBSC), $Ba_{0.5}Sr_{0.5}Co_{0.8}Fe_{0.2}O_{3-\delta}$ (BSCF), $Ba_{0.5}Sr_{0.5}Co_{0.8-x}Zr_xFe_{0.2}O_{3-\delta}$ (x = 0.05−0.2) (BSCZF), $BaCo_xFe_yZr_{1-x-y}O_{3-\delta}$ (BCFZ), $La_{0.6}Sr_{0.4}Co_{0.2}Fe_{0.8}O_{3-\delta}$ (LSCF), $SrSc_{0.1}Co_{0.9}O_{3-\delta}$ (SSC), $(Pr_{0.9}La_{0.1})_2(Ni_{0.74}Cu_{0.21}Ga_{0.05})O_{4+\delta}$ (PLNCG), and $Ce_{0.8}Sm_{0.2}O_{2-\delta}$-$La_{0.8}Sr_{0.2}MnO_{3-\delta}$ (Sm doped Ce-LSM).[5−24] Between these compositions, LSCF is the most promising in terms of its long-term stability (e.g. maintain stable permeation fluxes during a 3000 h test and moderate resistance to CO_2).[21,25] Substantial past research has been aimed to develop compositions with very high intrinsic fluxes, most of which showed decaying performance as a function of time and, thus, the trade-off between permeability and stability. The present strategy, however, has shifted toward utilizing proven stable composition showing low intrinsic fluxes. Microstructure engineering is further employed to develop the robust composition into a specific thin film geometry or configuration with increased fluxes.[1] The final product, as a result, is expected to fulfill both long lifetime and high flux performance.

Oxygen transport through ionic transport membrane involves oxygen gas dissociation and association into oxygen ions (lattice oxygen) on the surfaces of the membrane and oxygen ionic diffusion through the bulk membrane.[3] Therefore, the oxygen permeation fluxes can be enhanced by improving (or reducing) the rate (or the resistance) of surface exchange and/or bulk diffusion. For a relatively thick membrane, bulk-diffusion normally limits the oxygen transport.[3] In this case, decreasing the transport path of oxygen by reducing the membrane thickness would be effective. In a thin membrane, on the other hand, surface exchange dominates the oxygen transport resistance. Therefore, surface modification such as increasing surface roughness and electrocatalyst (e.g., Ag and Pd) deposition on the surface can be used to enhance the surface reaction for enlarged oxygen fluxes.[8,9,15,16,19]

This work is aimed to illustrate such concept and demonstrate that combined microstructure modification and Ag or Pt catalyst deposition can be used to attain optimized oxygen transport through LSCF hollow fiber. Modifying the hollow fiber into honeycomb-type structure (as opposed to conventional asymmetric one) is initially utilized to reduce the oxygen transport path and enhance surface reaction on the inner circumference surface. With the gradual transition of the oxygen transport limit from bulk-diffusion to surface reaction, an enhanced surface reaction rate is further achieved with the assistance of Ag or Pt outer circumference surface coating.

2. EXPERIMENTAL SECTION

2.1. Preparation of LSCF Powder and Hollow Fibers. $La_{0.6}Sr_{0.4}Co_{0.2}Fe_{0.8}O_{3-\delta}$ perovskite powders were prepared through a sol−gel process, as described in more detail elsewhere.[17] The oxide powder precursor was calcined at 800 °C for 3 h to remove residual carbon and to form the desired structure, ball-milled for 48 h in an agate jar, and sieved through a 200-mesh sieve. Hollow fiber membranes were fabricated by the phase inversion and sintering technique, as detailed elsewhere.[17] In short, the spinning solution consisted of 62.98 wt % LSCF powders, 6.30 wt % polyethersulfone (PESf) ((Radel A-300), Ameco Performance, U.S.A.), 25.18 wt % 1-methyl-2-pyrrolidinone (NMP) (AR grade, >99.8% purity, Kermel Chem Inc., Tianjin, China) as solvent, and 3.71 wt % polyvinyl pyrrolidone (PVP, K30) (AR grade, MW = 10,000, Fuchen Chem Inc., Tianjin, China) and 1.85 wt % deionized (DI) water as a nonsolvent additive. According to the triangular phase diagram of PESF, NMP, and the water system, the presence of water in a small concentrations less than 5 wt % will not cause the polymer precipitation but will change the solvent exchange rate from polymer phase to the internal and external coagulants.[26] The internal coagulant during spinning was a mixture of 10 wt % H_2O-90 wt % NMP, while tap water was used as the external coagulant. For conventional hollow fiber preparation, both of the internal and external coagulants were from pure water. The resultant hollow fiber precursors were then dried; cut in short lengths of 12 cm, and sintered to 1350 °C for 4 h using a ramping and cooling rate of 2 °C min^{-1} in stagnant air atmosphere to obtain gastight membranes. Disk membranes were also prepared as a baseline reference in oxygen fluxes results by pressing oxide powders in a KBr die module (15.0 mm in diameter) under a hydraulic pressure of approximately 1.5×10^8 Pa; followed by sintering to 1350 °C in stagnant air for 4 h using a ramping and cooling rate of 2 °C min^{-1}.

2.2. Surface Modifications. To enhance hollow fibres' surface reaction rate, silver (Ag) paste (PC-Ag-8100 supplied by Sino-Platinum Metals Co. Ltd., China) or platinum (Pt) paste (Pt−I-10 supplied by fuelcellmaterials.com) was applied to the outside surface of the hollow fibres (with effective length of 5 cm) using a paint-brushing technique. The coated hollow fibres were then heated to 800 °C for 2 h using a ramping rate of 5 °C min^{-1} to remove the organic resin from the paste and attach the metal particles onto the membrane surface.

2.3. Characterization. Viscosity of the spinning solutions were quantified using Physica UDS-200 rheometer at room temperature. Morphology and microstructure of the hollow fiber membranes were characterized by using scanning electron microscopy (SEM) (Zeiss EVO 40XVP). Gold sputter coating was performed on the samples under vacuum prior to SEM imaging. Powder X-ray diffraction (XRD) patterns were obtained using an X-ray diffractometer (PANalytical X'Pert PRO MPD) using a Cu Kα monochromatized radiation source and a Ni filter in the 2θ range 10−80°.

2.4. Oxygen Permeation Test. Oxygen permeation test was performed by placing the hollow fiber between two quartz tubes inside a tubular furnace while exposing the outside surface to ambient air with helium as sweep gas on the lumen side (Figure 1a). Prior to this,

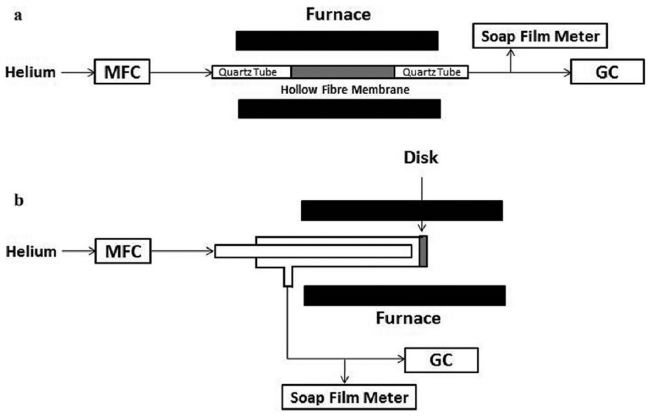

Figure 1. Schematic graph of the oxygen permeation apparatus: (a) hollow fiber module and (b) disk membrane module.

the gas-tightness of the hollow fiber was verified by observation, for example, gas bubble formation from outer hollow fiber surface when pressurized using 2 bar compressed air (during immersion in water). Oxygen permeation test for disk membrane was performed by sealing the disk onto a dense quartz tube using silver paste (Figure 1b) and preheating at 900 °C, as detailed elsewhere.[27] An effective disk area of 0.45 cm^2 was exposed at the sweep side for permeation study. High temperature (e.g., 750−950 °C) permeation experiments were conducted using helium gas sweep at flow rate between 50 and 150 mL min^{-1}. The composition of the permeate stream was analyzed using a Shimadzu GC-2014 with a 5A molecular sieve column and TCD detector. The permeate flow rate was measured by a bubble flow meter. The hollow fibres' ends were sealed with silver paste followed by heating to 900 °C. The sealing procedure was repeated at least

dx.doi.org/10.1021/ef300542e | Energy Fuels 2012, 26, 4728−4734

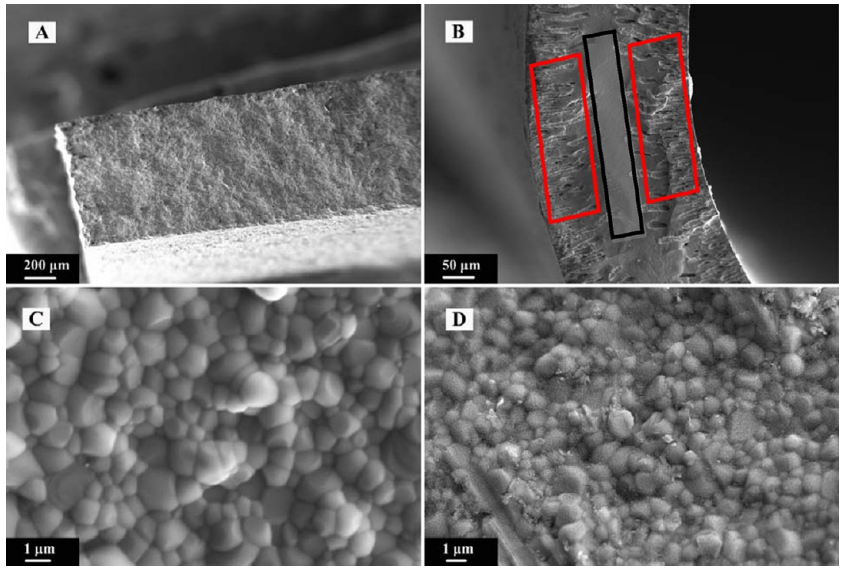

Figure 2. SEM images of disk membrane (A) and conventional LSCF hollow fiber (B–D). (B) fiber wall; (C) inner surface; (D) outer surface.

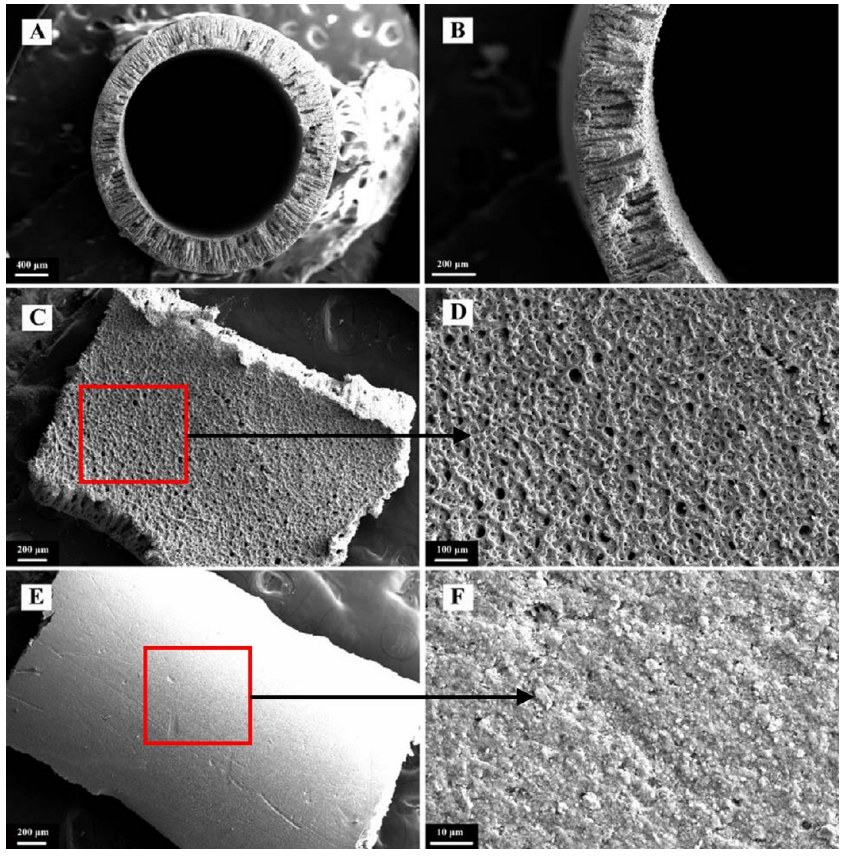

Figure 3. SEM images of LSCF hollow fiber precursor made using 10 wt % H_2O-90 wt % NMP as the internal coagulant. (A) cross section; (B) fiber wall; (C, D) inner surface (E, F) outer surface.

twice until nitrogen could no longer be detected. The air leak rate was <0.5%, below the minimum detection limit of the Shimadzu GC-2014.

3. RESULTS AND DISCUSSION

Figure 2A depicts the cross section of the disk membrane. The disk membrane has a dense structure with a relatively larger thickness of 1 mm, which is not favorable for oxygen transport considering its major bulk-diffusion resistance. Conventional hollow fiber can be fabricated using a combined phase inversion and sintering technique to reduce this membrane limitation. When water is used as both the internal and external coagulant, the resultant hollow fibres normally exhibit a sandwich cross-section structure consisting a dense layer in the center (marked with black box in Figure 2B) and finger-pore-like porous layers in the outer parts (marked with red boxes in Figure 2B). The hollow fiber has an apparent thickness of 0.3 mm. Dense

dx.doi.org/10.1021/ef300542e | *Energy Fuels* 2012, 26, 4728–4734

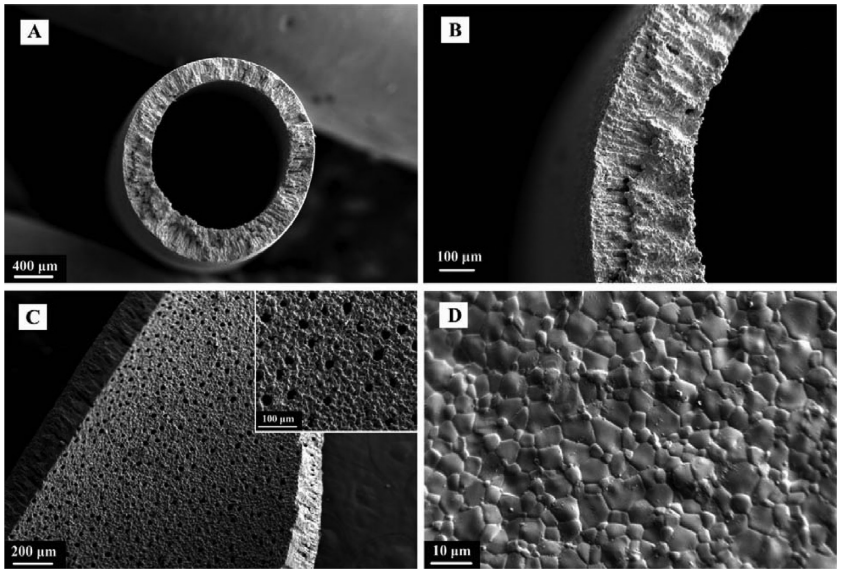

Figure 4. SEM images of sintered (1350 °C for 4 h) LSCF hollow fiber membrane made using 10 wt % H_2O-90 wt % NMP as the internal coagulant. (A) cross section; (B) fiber wall; (C) inner surface; (D) outer surface.

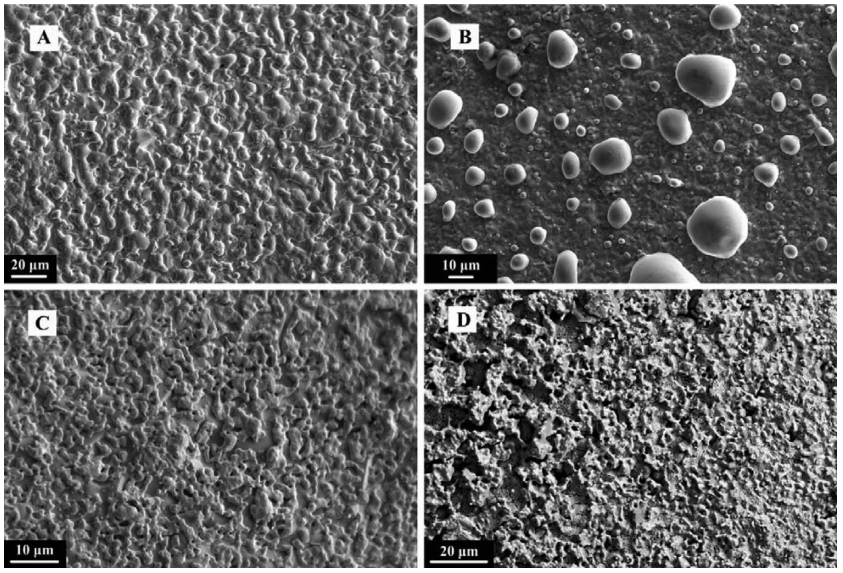

Figure 5. SEM images of outer surface of Ag-modified (A, B) and Pt-modified (C, D) honeycomb-structured LSCF hollow fiber membrane before (A, C) and after (B, D) oxygen permeation test.

surfaces, nonetheless, are noted on the inner and outer hollow fiber circumferences (Figures 2C and D). A decrease in thickness (relative to disk) is envisaged to improve the oxygen flux. Still, the porous cross-sectional structure containing multi-dense-layers in series tends to cause extra bulk-diffusion resistance, as well as creating the oxygen molecules trap inside the isolated pores. The formation of such a sandwich structure is due to the fast solvent (NMP) exchange rate from the polymer phase to aqueous phase. During the hollow fiber spinning process, the volume of internal coagulant being used is very minimal, only $^1/_{1000}$ of the volume of external coagulant. Changing the composition of the internal coagulant is a very good strategy to obtain novel hollow fibres with better morphology.

Figure 3 shows the SEM images of LSCF hollow fiber precursor made using the internal coagulant with a composition of 10 wt% H_2O-90 wt% NMP, which was demonstrated by previous studies to bring about the honeycomb-type membrane structure.[28] The outer and inner diameters of the fiber precursor are 2.92 and 2.18 mm, respectively (measured from Figure 3A). Figure 3B shows that the dense and finger-like structures in the inner layer of the cross-section (previously noted in Figure 2B) do not exist. Instead, the finger-like structure from the outer part of the cross-section is extended and slightly enlarged to the inner circumferences with a thin sponge layer formation on the outer surface of the hollow fiber precursor. The formation of this asymmetric structure is attributed to the slower polymer phase inversion process. Due to the high concentration of NMP, the solvent diffusion rate from the inner surface polymer phase to the aqueous phase is retarded relative to the pure water as the coagulant. As a result, the finger-like pores formed during coagulation are elongated to the inner surface of the hollow fiber precursor. Moreover, Figures 3C and D show that the inner circumference surface of

dx.doi.org/10.1021/ef300542e | *Energy Fuels* 2012, 26, 4728−4734

the hollow fiber precursor consists of numerous small pores. The outer circumference surface (Figures 3E and F), on the other hand, shows the formation of denser body without open pores.

Figure 4 shows the SEM images of the sintered (1350 °C for 4 h) hollow fiber membrane made using 10 wt % H_2O-90 wt % NMP as the internal coagulant. Substantial shrinkage occurred due to the removal of organic components and ceramic sintering (compare Figures 3A and 4A). The axial shrinkage of the hollow fiber membrane after sintering is close to 37%, and the outer and inner diameters of the sintered fiber become 1.99 and 1.43 mm, respectively. The morphology of the fiber precursor, nevertheless, is maintained after the sintering process (Figure 4B). Figure 4C reveals hollow fiber's inner circumference surface, showing honeycomb structure formation containing a large amount of uniform circular pores with diameters between 20 to 25 μm. The hollow fiber forms a dense structure on its outer circumference surface with well-defined grains in the order of 1−10 μm (Figure 4D). Thus, the sintered fiber exhibits only one dense layer near the outer cross-section layer followed by a porous finger-like layer in the middle, which extends to the inner cross-section layer. This microstructure is expected to reduce substantially the oxygen transport path (as well as the membrane thickness).

SEM images of the outer circumference surface of Ag and Pt deposited honeycomb-structured LSCF hollow fiber before and after oxygen permeation test are shown in Figure 5. After heat treatment at 800 °C, the organic component in Ag and Pt paste is removed while Ag and Pt particles were evidently anchored onto the surface (Figure 5A and C). After oxygen permeation testing up to 950 °C, Ag particles seem to be detached and aggregated independently on the surface forming larger Ag particles (Figure 5B) due to the melting of Ag at 962 °C.[29] In the case of Pt, such a phenomenon is not observed with a relatively similar coating layer remains (Figure 5D) because of higher melting point of Pt.[30] This aggregation and detachment is detrimental to oxygen surface reaction since it reduces the surface area per Ag unit volume in higher temperature operation (>950 °C). However, the oxygen permeation flux through the dense mixed conducting membranes is jointly determined by bulk diffusion rate and surface reaction kinetics. The bulk diffusion rate and reaction rate can be improved by the temperature increase. Despite the negative effect of catalyst (i.e., Ag) agglomeration, increased temperature may still spur the oxygen flux to a higher value considering its promoting effects on the bulk diffusion rate and reaction rate, which will be confirmed shortly.

Powder X-ray diffraction patterns of the honeycomb-structured LSCF hollow fiber sintered at 1350 °C are shown in Figure 6a. The characteristic peaks of the rhombohedral perovskite phase are denoted at 2θ (hkl) of 22.94 (012), 32.73 (110), 40.14 (202), 46.80 (024), 58.11 (214), 68.49 (208), and 77.87 (128), which were detected as reported elsewhere.[31,32] In addition, no other phases except the rhombohedral perovskite phase were observed in the used membrane after high temperature permeation test with XRD spectrum showing in Figure 6b. This features its relative higher stability at least under the experimental conditions. It should be noted that LSCF material is not absolutely stable at high temperatures to withstand the erosion of acid gases like CO_2 in the atmosphere. For example, after longer time operation over 3000 h, some impurity phases would be observed.[25] Ag or Pt deposition onto LSCF hollow fibres leads to the presence of extra reflections

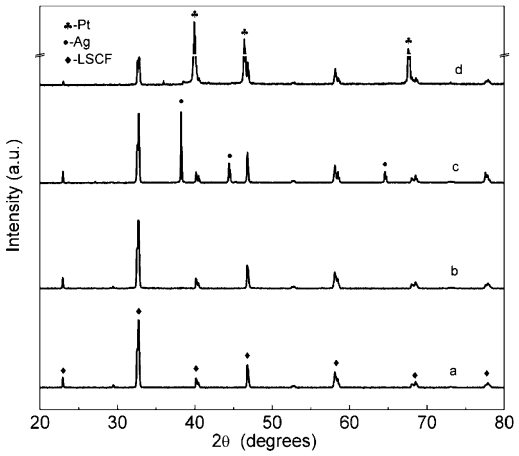

Figure 6. XRD patterns of the honeycomb-structured, used and modified LSCF hollow fiber. (a) honeycomb-structured fiber; (b) used honeycomb-structured fiber after oxygen permeation test; (c) the fiber modified by Ag paste; (d) the fiber modified by Pt paste.

assigned to the characteristic peaks of Ag or Pt metal (Figure 6c and d).

Figure 7 displays the oxygen permeation fluxes as a function of temperature between 750 and 950 °C at 100 mL min^{-1}

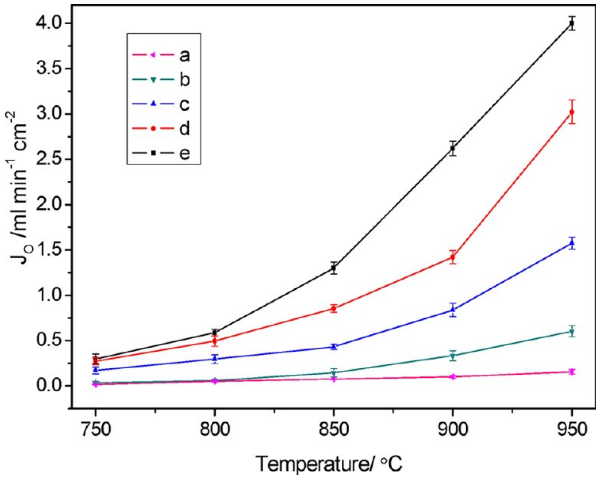

Figure 7. Oxygen permeation fluxes against temperature through disk membrane (a), conventional LSCF hollow fiber membrane (b), LSCF hollow fiber membrane with honeycomb structure (c), and LSCF hollow fiber membranes with honeycomb structure modified by Ag (d) and Pt (e) paste.

helium gas sweep rate for LSCF disk-shaped membrane, conventional LSCF hollow fiber membrane, LSCF hollow fiber membrane with honeycomb structure, and LSCF hollow fiber membranes deposited by Ag and Pt particles, respectively. The oxygen fluxes increase with increasing temperature due to the enhancement of oxygen ionic bulk-diffusion and surface reaction rates. The conventional hollow fiber with a sandwich structure performs better relative to the disk membrane, implying the major role of membrane geometry in oxygen transport. Membrane thickness reduction indeed enhances the oxygen transport. Furthermore, hollow fiber with a honeycomb structure provides better performance with respect to the conventional hollow fiber. This is because its particular microstructure containing a thin dense outer cross-section layer substantially contributes to decrease the bulk-diffusion

dx.doi.org/10.1021/ef300542e | Energy Fuels 2012, 26, 4728−4734

resistance by reducing the effective membrane thickness and increase the surface reaction rate by providing larger porous surface area (on inner circumference surface). The beneficial effect of depositing Ag and Pt is also verified in Figure 7. For example, at 950 °C and the sweep gas rate of 100 mL min^{-1}, the oxygen permeation flux is improved by 91.1% and 152.5% e.g. from 1.58 mL min^{-1} cm^{-2} to 3.02 mL min^{-1} cm^{-2} and 3.99 mL min^{-1} cm^{-2} in Ag and Pt case, respectively. This substantial improvement implies that the surface reaction limits the oxygen transport through the honeycomb-structured LSCF hollow fibres. In addition, these results also suggest that Pt is more effective than Ag which in this study might be attributed to higher activity of Pt in dissociation oxygen and the more homogeneous coating of Pt afforded by its higher melting point in comparison to Ag (Figure 5B and D). The excellent catalytic effects of Pt on other membrane materials like $SrFeCo_{0.5}O_x$ and $Ba_{0.5}Sr_{0.5}Co_{0.8}Fe_{0.2}O_{3-a}$ were also observed by other researchers.[33,34]

Figure 8 shows the effect of sweep gas flow rate on oxygen fluxes. The improvement of oxygen fluxes at increasing sweep

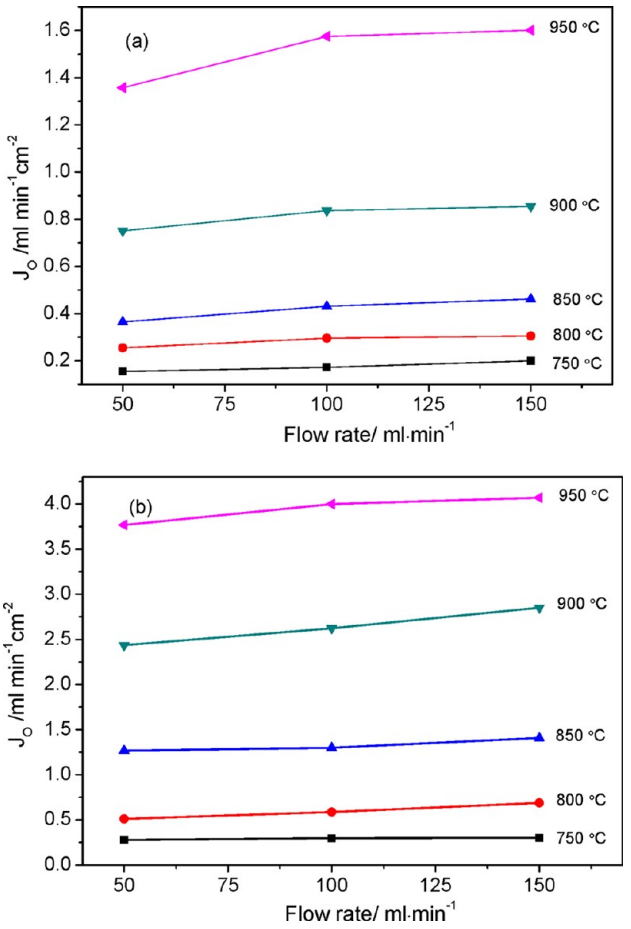

Figure 8. Effects of helium sweep rate on the on the oxygen fluxes through the honeycomb-structured LSCF hollow fiber (a) and the honeycomb-structured LSCF hollow fiber modified by Pt (b).

gas rate is related to enlarged oxygen partial pressure driving force, which arises from the lowering oxygen partial pressure in the permeate side. At the same sweep gas rate, Pt-deposited honeycomb-structured LSCF hollow fiber membrane demonstrates improved oxygen fluxes at similar operating temperatures compared to the nondeposited hollow fiber. The operating temperature seems to influence oxygen transport to a larger extent relative to the oxygen partial pressure driving force. For example, at 950 °C, increasing the sweep gas rate from 50 to 150 mL min^{-1} slightly raises the oxygen flux though Pt-deposited and nondeposited hollow fibres from 3.77 to 4.07 mL min^{-1} cm^{-2} and 1.36 to 1.60 mL min^{-1} cm^{-2}, respectively. Nonetheless, the oxygen flux though Pt deposited and nondeposited hollow fibres increases dramatically from 0.28 to 3.77 and 0.15 to 1.36 mL min^{-1} cm^{-2}, respectively, upon increasing the temperature from 750 to 950 °C at constant sweep gas rate of 50 mL min^{-1}. The observed oxygen flux value of 3.77 mL min^{-1} cm^{-2} of Pt-deposited hollow fiber membrane is the best value among the reported LSCF membranes under the gradient of air/helium (or other inert gases).

4. CONCLUSIONS

Good membrane materials with inherently higher oxygen permeation fluxes and sufficient material stability are very rare. In this work, based on $La_{0.6}Sr_{0.4}Co_{0.2}Fe_{0.8}O_{3-\delta}$ membranes, microstructure engineering and catalyst technologies were vividly displayed as good techniques to improve the oxygen permeation fluxes. The original flux of the disk-shaped membrane has been enlarged by factors of 3, 8, and 26 when the membrane geometry changed to conventional hollow fiber, honeycomb morphological hollow fiber, and Pt catalyst deposition, respectively. These technologies are particularly useful in the membrane field to fulfill the purpose of seeking long lifetime and high flux performance from robust material composition with inherently lower permeation fluxes.

AUTHOR INFORMATION

Corresponding Author

*Telephone: (86)532-86981296 (Z.Y.); (61)8-92669056 (S.L.). E-mail: zfyancat@upc.edu.cn (Z.Y.); shaomin.liu@curtin.edu.au (S.L.).

Notes

The authors declare no competing financial interest.

ACKNOWLEDGMENTS

The authors gratefully acknowledge the research funding provided by the Australian Research Council (DPs 0985578 and 110104599).

REFERENCES

(1) Czyperek, M.; Zapp, P.; Bouwmeester, H. J. M.; Modigell, M.; Ebert, K.; Voigt, I.; Meulenberg, W. A.; Singheiser, L.; Stöver, D. *J. Membr. Sci.* **2010**, *359*, 149−159.

(2) Leo, A.; Liu, S.; Diniz da Costa, J. C. *Int. J. Greenhouse Gas Control* **2009**, *3*, 357−367.

(3) Sunarso, J.; Baumann, S.; Serra, J. M.; Meulenberg, W. A.; Liu, S.; Lin, Y. S.; Diniz da Costa, J. C. *J. Membr. Sci.* **2008**, *320*, 13−41.

(4) Stiegel, G. J.; Maxwell, R. C. *Fuel Process. Technol.* **2001**, *71*, 79−97.

(5) Sunarso, J.; Liu, S.; Lin, Y. S. *Energy Environ. Sci.* **2011**, *4*, 2516−2519.

(6) Liu, S.; Gavalas, G. R. *J. Membr. Sci.* **2005**, *246*, 103−108.

(7) Liu, S.; Gavalas, G. R. *Ind. Eng. Chem. Res.* **2005**, *44*, 7633−7637.

(8) Leo, A.; Liu, S.; Diniz da Costa, J. C. *J. Membr. Sci.* **2009**, *340*, 148−153.

(9) Leo, A.; Smart, S.; Liu, S.; Diniz da Costa, J. C. *J. Membr. Sci.* **2011**, *368*, 64−68.

(10) Meng, X.; Yang, N.; Meng, B.; Tan, X.; Ma, Z.; Liu, S. *Ceram. Int.* **2011**, *37*, 2701−2709.

(11) Schiestel, T.; Kilgus, M.; Peter, S.; Caspary, K. J.; Wang, H.; Caro, J. *J. Membr. Sci.* **2005**, *258*, 1−4.
(12) Liang, F.; Jiang, H.; Schiestel, T.; Caro, J. *Ind. Eng. Chem. Res.* **2010**, *49*, 9377−9384.
(13) Tan, X.; Liu, Y.; Li, K. *Ind. Eng. Chem. Res.* **2005**, *44*, 61−68.
(14) Li, K.; Tan, X.; Liu, Y. *J. Membr. Sci.* **2006**, *272*, 1−5.
(15) Liu, H.; Tan, X.; Pang, Z.; Diniz da Costa, J. C.; Lu, G. Q.; Liu, S. *Sep. Purif. Technol.* **2008**, *63*, 243−247.
(16) Liu, H.; Pang, Z.; Tan, X.; Shao, Z.; Sunarso, J.; Ding, R.; Liu, S. *Ceram. Int.* **2009**, *15*, 1435−1439.
(17) Wang, Z.; Yang, N.; Meng, B.; Tan, X. *Ind. Eng. Chem. Res.* **2009**, *48*, 510−516.
(18) Tan, X.; Wang, Z.; Li, K. *Ind. Eng. Chem. Res.* **2010**, *49*, 2895−2901.
(19) Yacou, C.; Sunarso, J.; Lin, C. X. C.; Smart, S.; Diniz da Costa, J. C. *J. Membr. Sci.* **2011**, *380*, 223−231.
(20) Liu, N.; Tan, X.; Meng, B.; Liu, S. *Sep. Purif. Technol.* **2011**, *80*, 396−401.
(21) Tan, X.; Liu, N.; Meng, B.; Sunarso, J.; Zhang, K.; Liu, S. *J. Membr. Sci.* **2012**, *389*, 216−222.
(22) Meng, B.; Wang, Z.; Tan, X.; Liu, S. *J. Euro. Ceram. Soc.* **2009**, *29*, 2815−2822.
(23) Wei, Y.; Tang, J.; Zhou, L.; Li, Z.; Wang, H. *Ind. Eng. Chem. Res.* **2011**, *50*, 12727−12734.
(24) Li, W.; Tian, T. F.; Shi, F. Y.; Wang, Y. S.; Chen, C. S. *Ind. Eng. Chem. Res.* **2009**, *48*, 5789−5793.
(25) Schlehuber, D.; Wessel, E.; Singheiser, L.; Markus, T. *J. Membr. Sci.* **2010**, *351*, 16−20.
(26) Wang, D.; Li, K.; Sourirajan, S.; Teo, W. K. *J. Appl. Polym. Sci.* **1993**, *50*, 1693−1700.
(27) Sunarso, J.; Liu, S.; Lin, Y. S.; Diniz da Costa, J. C. *J. Membr. Sci.* **2009**, *344*, 281−287.
(28) Tan, X.; Liu, N.; Meng, B.; Liu, S. *J. Membr. Sci.* **2011**, *378*, 308−318.
(29) Tan, X.; Wang, Z.; Liu, H.; Liu, S. *J. Membr. Sci.* **2008**, *324*, 128−135.
(30) Wang, Z. L.; Petroski, J. M.; Green, T. C.; El-Sayed, M. A. *J. Phys. Chem. B* **1998**, *102*, 6145−6151.
(31) Waller, D.; Lane, J. A.; Kilner, J. A.; Steele, B. C. H. *Mater. Lett.* **1996**, *27*, 225−228.
(32) Kostogloudis, G.Ch.; Ftikos, Ch. *Solid State Ionics* **1999**, *126*, 143−151.
(33) Murphy, S. M.; Slade, D. A.; Nordheden, K. J.; Stagg-Williams, S. M. *J. Membr. Sci.* **2006**, *277*, 94−98.
(34) Leo, A.; Liu, S.; Diniz da Costa, J. C.; Shao, Z. *Sci.Technol. Adv. Mater.* **2007**, *7*, 819−825.